Contrails Measurement and Testing Capabilities in NASA's Particulate Aerosol Laboratory

Amy F. Fagan[1], Francisco J. Guzman[2], Derek P. Podboy[3], Martin J. Rabinowitz[4], Kevin D. Brusk[5]
NASA Glenn Research Center, Cleveland, Ohio, 44135, USA

Devin M. Podboy[6], Richard C. Newport[7]
HX5 Sierra, Cleveland, Ohio, 44135, USA

Brett A. Thomascik[8], Kristie A. Elam[9], Seth J. Caldwell[10]
Jacobs Technology, Cleveland, Ohio, 44135, USA

The NASA Glenn Research Center Particulate Aerosol Laboratory (PAL) is a ground test facility for studying emissions and contrails at upper atmospheric conditions. The facility consists of a small-scale combustor that generates hot combustion gases and soot nanoparticles, which flow through a transition pipe into a jet nozzle, which exhausts into an altitude chamber. Thermodynamic conditions experienced in flight are matched in the altitude chamber, allowing the study of ice particle formation of simulated aircraft engine exhaust plumes. A non-intrusive optical diagnostic technique based on Mie scattering provides ice particle size, number density, and mass density. A suite of commercial extractive particle measurement instruments provides estimates of soot number density, size, and black carbon mass distributions. Measurements are presented for various fuels at chamber conditions covering an altitude range of 20,000 ft (6 km) to 45,000 ft (14 km) altitude and ambient temperatures from -48°C to -68°C. The data presented demonstrate the effect of soot number density, altitude, and fuel-to-air equivalence ratio on the contrail ice particle formation. Ice mass density measurements are compared to values predicted by a thermodynamic plume similarity solution.

I. Introduction

A contrail is an aircraft condensation trail composed of ice particles that form in the exhaust of the aircraft when flying in the upper atmosphere. The physics of this formation process are still not completely understood. Contrails are a major concern related to global warming since they may persist as cirrus clouds and increase the effective

---

[1] Research Engineer, Optics and Photonics Branch, AIAA Associate Fellow
[2] Research Chemical Engineer, Engine Combustion Branch
[3] Mechanical Engineering Technical Lead AAPL and Flow Physics, Aviation Test Branch
[4] Senior Physicist, Engine Combustion Branch
[5] Mechanical Engineering Technician, Aviation Test Branch
[6] Mechanical Test Engineer, Aviation Test Branch
[7] Research Lab Technician, Aviation Test Branch
[8] Electrical Engineer, Aviation Test Branch
[9] Data Systems Engineer, Data and Systems Branch
[10] Research Lab Mechanic, Aviation Test Branch

radiative forcing [1,2]. Sustainable aviation fuels (SAF) can decrease contrail formation since they produce fewer soot particles due to their lower aromatic content [3,4]. Studying the composition and formation of contrails in flight is difficult due to the lack of instrumentation and the high cost of flight tests. Testing contrail formation in altitude chambers is therefore an important cost-effective alternative. To this extent, the Particulate Aerosol Laboratory (PAL) at NASA Glenn Research Center (GRC) is a ground test facility aimed at evaluating aircraft emissions and contrail formation. The PAL consists of a small-scale combustor that generates the hot combustion gases and soot, which flow through a heated transition pipe to the nozzle, which exhausts into the altitude chamber. Thermodynamic conditions experienced at upper tropospheric flight regimes are matched to study the soot and ice particulates of simulated aircraft engine exhaust plumes. Extractive non-volatile particulate instruments along with a non-intrusive Mie scattering diagnostic provide a suite of diagnostics to characterize the soot and ice particles in exhaust plumes in the PAL facility. PAL has had many upgrades and improvements since it was reported on in [5,6], such as a cleaner burning combustor, a heated spray chamber with improved atomization, and upgraded diagnostics and instrumentation having better signal-to-noise and measurement accuracy. The goal of this paper is to provide a detailed overview of the facility and its capabilities while presenting some representative measurements of the soot and contrail ice particulates.

II. Facility

Photographs of the Particulate Aerosol Laboratory (PAL) are shown in Fig. 1. PAL has been in continuous operation since 2006 and was designed to study aviation emission exhaust plumes at conditions relevant to upper tropospheric flight corridors. In this unique facility, a combustor capable of burning conventional and alternative jet fuels exhausts into an altitude chamber that simulates the temperature and pressure conditions up to 45,000 ft (14 km). This allows researchers to study particle evolution at altitude at a fraction of the cost associated with flight testing. The facility is designed to be highly configurable. It utilizes a swirl-atomized combustor, a heated transition pipe, and a small-scale jet exhaust nozzle housed in an altitude chamber. The exhaust emission flow path from the combustor proceeds through a transition pipe (2.43 cm diameter, 160 cm length). It is then injected upwards through an adjustable diameter scaled nozzle (generally 1.8 cm diameter) into an altitude chamber with a temperature and pressure environment corresponding to aircraft cruising altitudes.

The cylindrical altitude chamber is 0.6 m in diameter and 1.8 m long and can simulate a wide range of altitude conditions anywhere from sea level to 45,000 ft [ambient pressure from 101 kPa (14.7 psia) to 14.5 kPa (2.1 psia)]. The chamber temperature range is room temperature to -79°C and is controlled by liquid nitrogen (LN2) supplied from a 3000-gallon dewar. The LN2 passes through a series of electric heaters, converting the working fluid of the chamber into gaseous nitrogen (GN2). The GN2 enters the altitude chamber manifold at the bottom of the chamber and is regulated by a diaphragm-operated control valve. It then passes through a pair of screens followed by a honeycombed flow straightener that conditions the flow at a maximum rate of 6 lb/sec. The background GN2 and combustion products co-flow together and exit the chamber through an exhaust duct at the top of the chamber. Since the thermodynamic characteristics of GN2 are not different from air it is acceptable to use GN2 as the co-flow. The exhaust duct is coupled to a high-flow vacuum source provided by GRC's Central Process Systems altitude exhaust. It consists of an extensive, centralized vacuum system providing continuous sub-atmospheric pressures that mimic upper tropospheric conditions. This system can provide flow rates up to 6 lb/sec and is regulated by an electro-hydraulic actuator. The chamber incorporates four vertical ports for multiple instrumentation and diagnostic configurations. Two 152 cm tall by 10.2 cm wide port hole plates are opposite each other and contain eleven port holes each measuring 6.35 cm in diameter. These port holes can be used for instrumentation installations and various port hole window glass options. The two opposing ports clocked 90° from the instrumentation port hole plates contain Starphire® glass double-paned window assemblies, also 152 cm tall and 10.2 cm wide, to provide access for optical diagnostic measurements. The space between the two panes of glass is evacuated to prevent condensation or ice build-up on the windows. Room temperature air is also blown on the exterior surfaces of all chamber windows for additional protection against condensation. The optical measurement plane can be adjusted, ranging from near the nozzle exit plane to 1.2 m from the nozzle by translation of the optical diagnostic components (lenses and fibers) along the windows on a rail system. This allows for ice particle diagnostics, including wavelength-resolved optical absorption and scattering, which can achieve accurate sizing and number density measurements for ice particles > 50 nm diameter and ice water content > 0.04 g/m^3.

PAL's combustor is an air-assist pressure blast atomizer simulating aircraft exhaust during cruise conditions. The combustor produces emissions with typical particulate size distributions (10-25 nm) and number densities (~1.2x10^7 #/std.cm^3) that resemble current jet engines. If desired, a suite of non-volatile particulate measurement equipment is available to acquire particulate samples from the combustion zone. The fuel and air are supplied separately into the injector, and mixing occurs downstream of the nozzle orifice. Air is delivered at a relatively high velocity to break up the fuel jet and disperse the resulting spray in the combustion zone. This creates fuel atomization of tiny droplets with a large surface area-to-volume ratio, producing effective combustion performance. The maximum temperature the combustor can achieve is 525°C. Fuel flow rates can range from 1.8 mL/min up to 10 mL/min and are supplied by a standard Jet-A pump or alternative fuel pump. The two fuel systems can be switched in real-time, allowing continuous burner operation while modifying fuel composition. The standard fuel delivery system incorporates dual 500 mL syringe pumps. These fuel pumps provide constant flow with precise accuracy for extended periods.

A transition pipe spans the combustor to the nozzle exit. It measures 2.43 cm in diameter and 160 cm in length. It contains configurable orifices of various sizes that drop the pressure from the combustion products near the pressure of the altitude chamber. Several axially spaced port holes are present to introduce instrumentation, sampling probes, chemical additives, and supplemental heat. Heat tape and insulation reduce the thermal losses between the combustor and nozzle exit. Heated spray chambers can be added to introduce varying amounts of simulated combustion products (e.g., water vapor). Syringe pumps control the quantity of artificially introduced combustion products into the spray chamber via atomizers. If additional heat is required aft of the combustor, a 6kW in-line electric heater is available to provide supplemental heat to the transition pipe up to 815°C. The heater can be configured to supplement the combustion-heated primary flow or to replace the combustor as the primary heat source. The latter use allows for studying homogeneous nucleation since the soot source is removed.

The Particulate Aerosol Laboratory allows for studies of the thermodynamic state of contrail formation as a function of fuel composition at realistic flight conditions. A calibrated thermodynamic prediction code integrated with the facility data system enables real-time estimates of the chamber conditions. Schematics of the facility, the transition pipe, and the combustion chamber are shown in Figs. 2-4. A color camera is mounted in a port looking into the combustion chamber along with a fire eye. Sample images of flames observed for Jet-A and a cleaner burning sustainable alternative fuel are shown in Fig. 5.

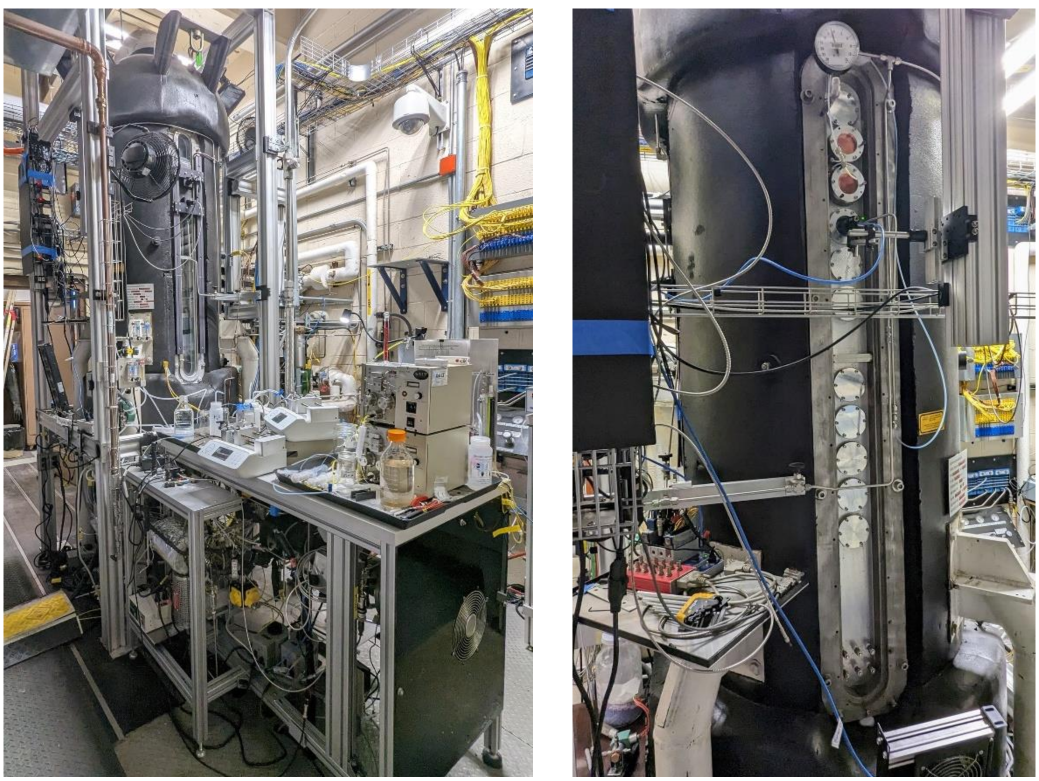

Fig. 1. Photos of the Particulate Aerosol Laboratory. The table in for foreground of the photo on the left contains the syringe pumps; the combustion chamber and transition pipe reside beneath this table. The photo on the right depicts the instrumentation port hole plate with a color camera installed in the third port from the top.

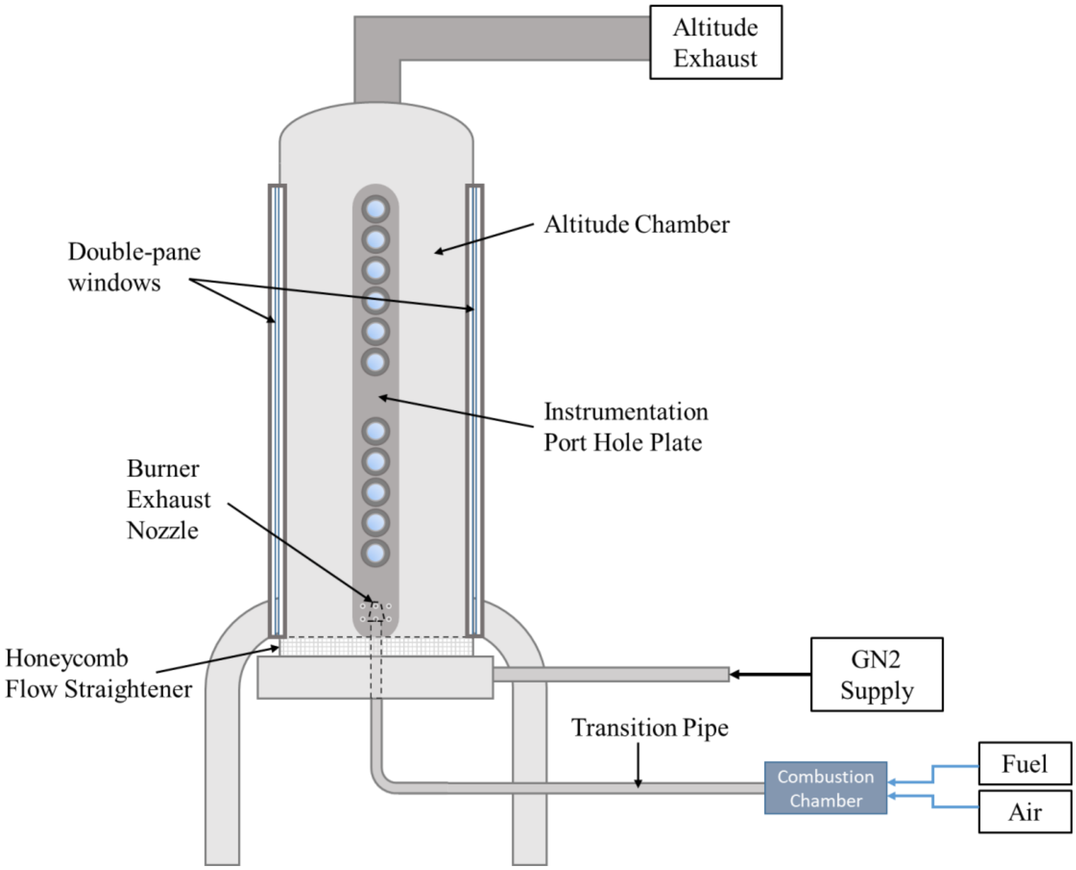

Fig. 2. Schematic of the PAL facility

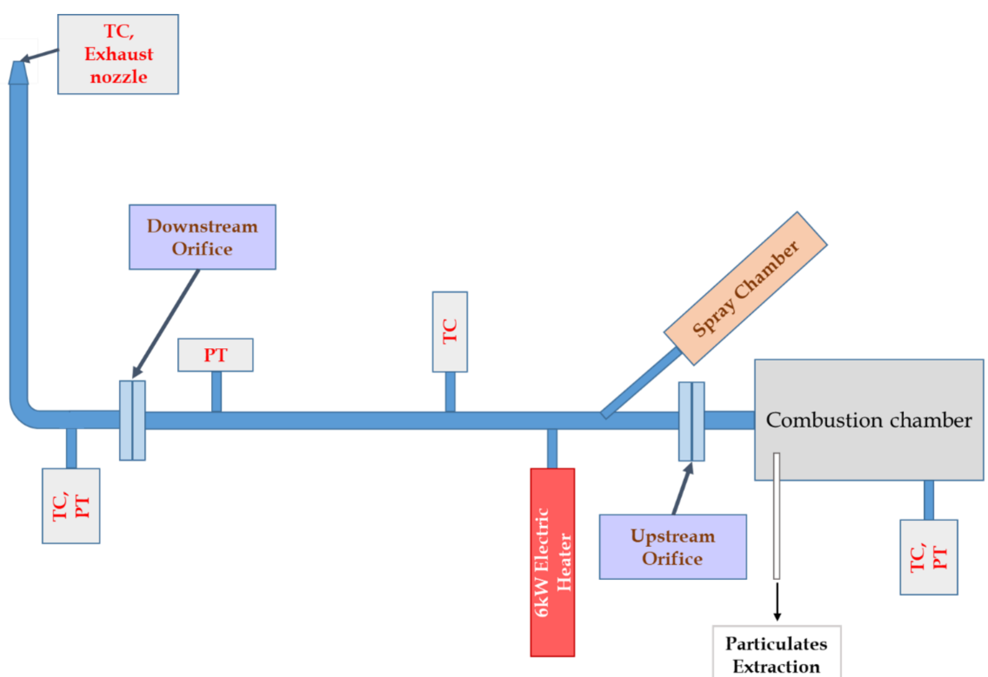

Fig. 3. Schematic of the transition pipe spanning the length from the combustion chamber to the exhaust nozzle that feeds the combustion gases into the altitude chamber; TC=Thermocouple, PT=Pressure Transducer.

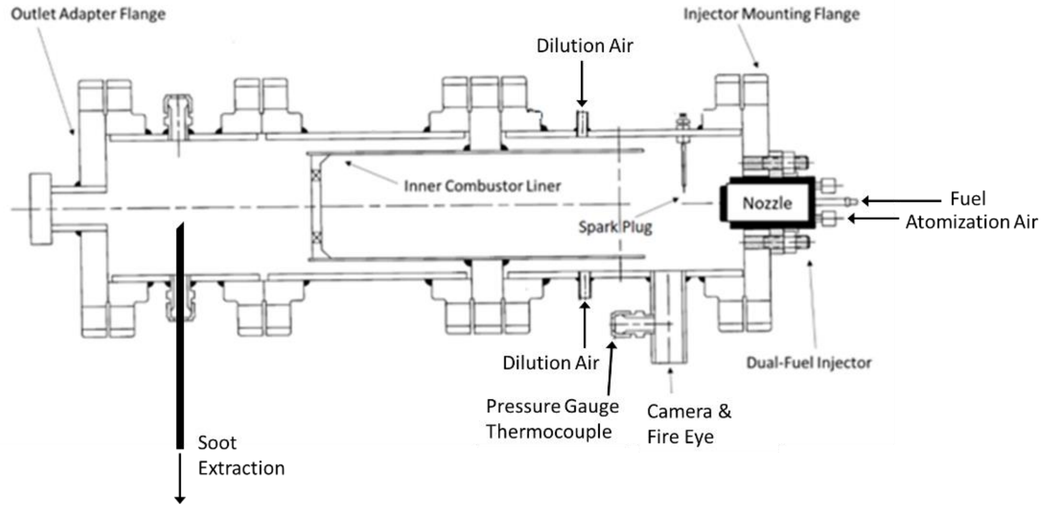

Fig. 4. Schematic of the PAL combustion chamber.

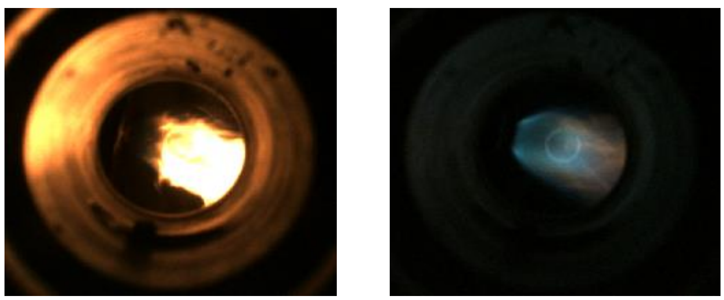

Fig. 5. Images of typical flames from Jet-A (left) and sustainable aviation fuels (right) in the PAL combustion chamber. Flow is left to right. The circular shaped object that can be seen through the blue flame is the spark plug mounted on the opposite side of the chamber from the camera.

III. Ice Particle Diagnostics

The ice particle diagnostics consist of a Mie scattering absorption and scattering measurement system that provides a path-integrated measurement of the mean particle diameter and number density of an assumed log-normal unimodal size distribution. A schematic of the optical system installed on the windows of the PAL chamber is shown in Fig. 6. The optical system components and data processing are described in this section.

A. Experimental Setup

The light source for the Mie scattering diagnostic is a six-wavelength light emitting diode (LED) source that provides illumination over the wavelength range from 360nm to 650nm. Two different light source models are available with slightly different LED options. The spectral output of the two options is shown in Fig. 7. Only five of the six LEDs of source A could be used because the output of the longest wavelength LED (λ=780nm, not shown) was very unsteady. LED source B provides more data at shorter wavelengths which is ideal for this diagnostic due to its increased sensitivity to particle size at wavelengths less than 450nm. Data from both sources are presented in this paper. The light source is mounted in a thermally controlled environmental box to keep the spectral output steady, minimizing error in the Mie scattering measurements. A 3mm diameter liquid light guide transmits the light from the source to a fused-silica 90-mm focal length lens that provides a 25mm collimated beam through the test section. The light source and associated collimating optics are shown in the inset photo in Fig. 6. An identical lens on the opposite side of the chamber collects the transmitted light and sends it via 200μm diameter optical fiber to an Ocean Insight FLAME-S model spectrometer to spectrally resolve the signal. First, a 'reference' signal, I_{ref}, with no exhaust plume present, and a 'dark' signal, I_{dark}, with the light source off are acquired. Then, the signal, I, is acquired when the source beam passes through the exhaust plume under study; the ice particles scatter and absorb some of the light. The transmission, T, is calculated by the following equation:

$$T = \frac{I - I_{dark}}{I_{ref} - I_{dark}} \tag{1}$$

Two similar collection lens systems are mounted on the windows as shown in Fig. 6, to collect the forward-scattered (16°) and back-scattered (164°) light. These scattering signals are transmitted via 400µm diameter optical fibers and spectrally resolved by identical FLAME-S spectrometers that are calibrated for absolute irradiance measurements. Not shown in the schematic is a color camera that images the 25mm beam from a 90° observation direction. The camera can be seen mounted on one of the window ports in Fig. 1(b). The data recorded by the spectrometers are analyzed with a custom optimization program that fits a model function to the transmission spectrum to extract mean particle size and number density. Using optical transmission for measuring particle size and concentration has been widely used for decades [7-9], and while it has some limitations [10], this paper demonstrates that it works well in the scattering regime typical of the PAL ice particulates. When the particles get very large (>2000nm) the transmission curves are quite flat and there can be many possible solutions. In these cases, it will be helpful to utilize the ratio of forward-to-back scattering as an additional parameter for fitting the particle size. The forward and back-scattering signals have only been used for rough analysis in the current work since the back-scattering signal is corrupted by significant forward scattered signal from the reflection of the incident light beam off the two glass windows on the opposite side of the chamber. The forward scattering is likewise corrupted by the backscattering from the reflected beam; however, the backscatter signal is much weaker than the forward scattering and likely does not have any significant effect. We are investigating ways to calibrate the scattering signals to account for these additional contributions. The optical system is mounted on rails so it can easily be moved to any distance from 0 to 1.2 m downstream of the nozzle exit.

B. Mie Scattering Data Analysis

The data analysis is based on Mie scattering theory [11] and MATLAB subroutines for calculating the theoretical Mie scattering coefficients provided by Mätzler [12]. The transmission signal is related to the absorbance, A, which is a function of the extinction coefficient, Q_{ext}, and an integration over the particle size distribution (*psd*) for particles of radius, r. Multiplying the integral by the number density of ice particles, N_{ice}, and the path length through the exhaust plume, L, gives the total measured absorbance. Transmission, T, is a function of the absorbance.

$$A = N_{\mathrm{ice}} L \int_0^\infty Q_{ext}\, \pi r^2 (psd) dr \tag{2}$$

$$T = e^{-A} \tag{3}$$

The extinction coefficient, Q_{ext}, and the scattering amplitudes, *S1* and *S2*, are functions of the mean particle diameter, D_{ice}, the width of the size distribution, σ, the wavelength of the illumination, λ, and the refractive indices of the particles (n_{ice}) and the surrounding medium (n_{medium}). The spectrally resolved transmission signals are fit to a numerical model, which assumes a log-normal size distribution with a 30% standard deviation, to provide mean particle size, D_{ice}, and number density, N_{ice}. The length L is estimated from the camera images. The ice mass density (units: g/m^3) is calculated from the measured D_{ice} and N_{ice} values, the width of the plume, L, and the associated log-normal size distribution. The model function assumes a unimodal size distribution of spherical particles. The index of refraction is assumed to be that of pure ice and does not account for changes in index of refraction with temperature, which should be small. A 30% standard deviation in the size distribution is an acceptable value based on contrail ice measurements in the literature and that it typically provides a good fit to the data. However, the standard deviation can be adjusted to other values, if desired. Sample experimental transmission data for various mean ice particle sizes are shown in Fig. 8. These data were acquired at a measurement plane of x=1.15 m and at altitudes of 30,000 ft to 40,000 ft (9 km to 12 km), ambient temperatures of -48°C to -68°C, and nozzle exit temperatures ranging from 90°C to 150°C. A sample log-normal size distribution for 500nm particles with a 30% standard deviation is shown in the inset of Fig. 8 to demonstrate what a typical distribution assumed by the model function (Eq. 2). The shape and overall amplitude of the transmission as a function of wavelength are dictated by the size and number of particles in the illuminated path through the exhaust plume. The sections of the spectrum where data are lacking are the regions where there is no signal between the LED peaks (see source spectrum shown in Fig. 7). The data for particles sizes of 362, 469, and 679 nm were acquired with LED Source A, while the data for particles sizes of 267, 949, 1014, 1177, and

2496 nm were acquired with LED source B. Small particles (<600nm) have continuously decreasing transmission with decreasing wavelength. As size increases the transmission curves upwards on both ends of the spectrum and eventually gets flat. The shape of the transmission spectrum is mostly governed by the size of the particles whereas the number of particles shifts the curve up or down. Sample images from the color camera that records the scattered light from a side view are shown in Fig. 9 for three different particle size distributions (D_{ice} = 362nm, 602nm, and 2496nm). The scattered light appears slightly bluer for the left two images because very small particles (diameter < wavelength of the light) scatter more in the blue end of the spectrum, which yields higher extinction or lower transmission in the signals at short wavelengths as shown in Fig. 8. As the size gets larger (> 1000nm) the particles scatter more uniformly across all wavelengths leading to a whiter plume image and a flatter transmission spectrum.

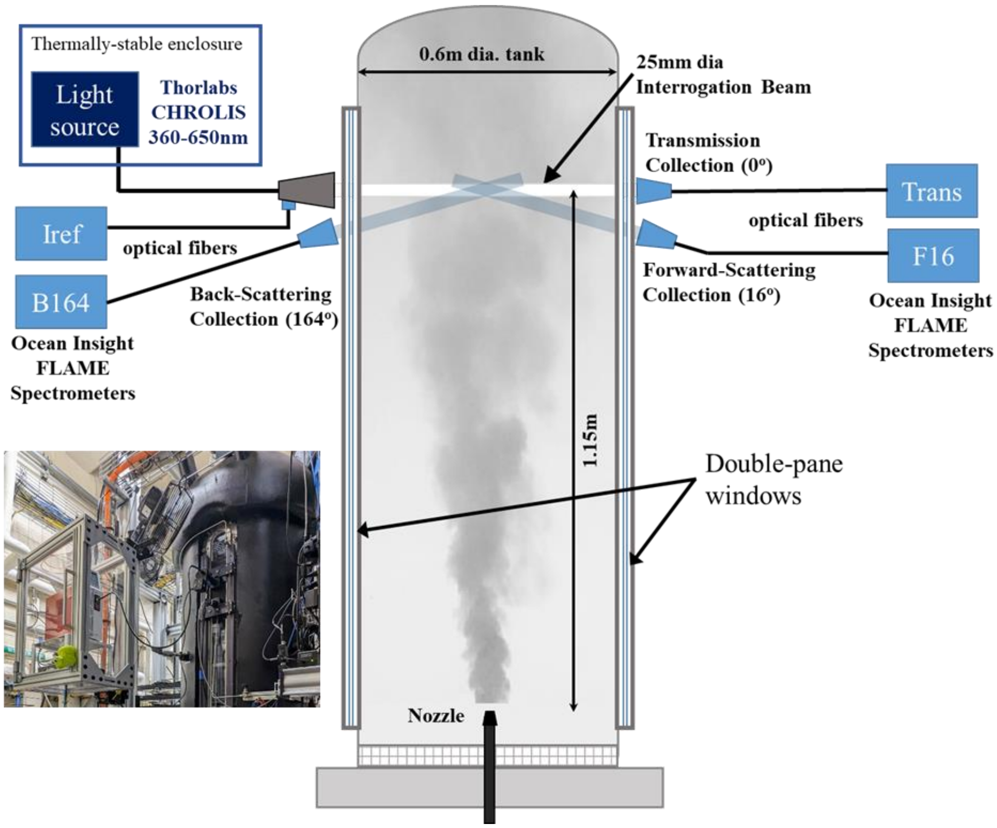

Fig. 6. Schematic of the Mie Scattering optical system installed in PAL. Inset photo shows the six-wavelength LED light source in the environmental box and the optics mounted on the chamber window.

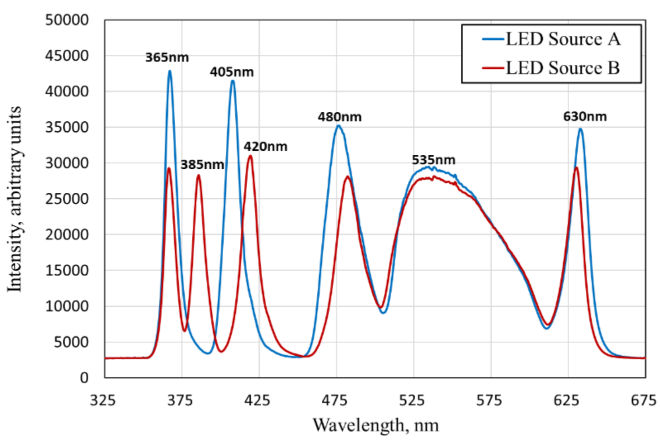

Fig. 7. Optical spectra of the CHROLIS light sources used for the Mie scattering diagnostic.

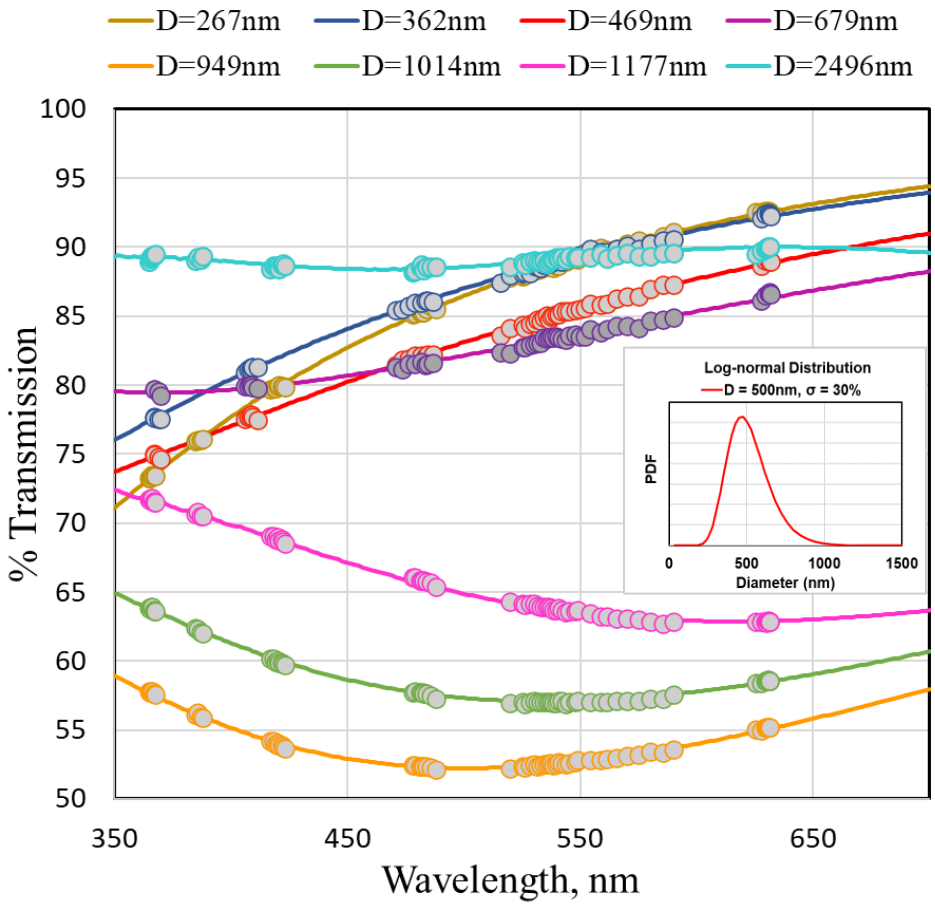

Fig. 8. Experimental transmission data (circle symbols) from ten different runs resulting in ice particle sizes with mean diameters from 267nm up to 2496nm and the resulting numerical model solutions from the Mie scattering analysis code (solid lines). The facility conditions and ice densities varied between runs. This plot illustrates the effect of mean particle size on transmission spectral shape and how well the model function fits the actual data. The inset figure shows a sample log-normal distribution with a 30% standard deviation, which is the assumed size distribution in the numerical model.

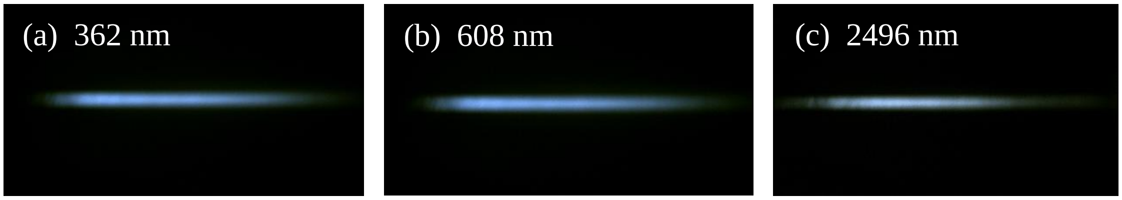

Fig. 9. Camera images of the illuminated plume observed from 90° for various sizes of ice particles.

IV. Soot Diagnostics

PAL includes a suite of non-volatile particulate matter (nvPM) measurement capabilities based on the SAE ARP6320A sampling procedure with samples taken from the combustion zone. A schematic of the sampling and dilution system is shown in Fig. 10. A thick walled 9.5mm stainless tube cut at 45° is aligned with the middle of the combustion zone. To minimize thermal losses, heat tape and heated hoses are used to maintain the sample as warm as possible prior to reaching the instrumentation. A flow orifice is used such that 80% of the dynamic pressure drop is taken at the orifice. A 3-way valve is used to purge the sampling system or route the sample into the nvPM and gaseous instrumentation. After the 3-way valve, a flow splitter is used for simultaneous gaseous and particulate sampling. For both the gaseous and nvPM sample lines a solenoid valve is used to open or close the flow. For the nvPM sample, the sample proceeds through a Dekati diluter, which as an ejection-type dilution system. The current gaseous emissions bench consists of a Siemens Ultramat 23 analyzer which measures CO and CO_2 by use of non-dispersive infrared radiation and O_2 by use of an electrochemical sensor.

Figure 11 shows a diagram of the Dekati diluter system. The Dekati diluter ensures rapid mixing of the sample which freezes the particle state, minimizes the deposition of particles within the diluter, and keeps the number densities below the saturation limit of the nvPM instruments. Particle and moisture free gaseous nitrogen is used as the diluent gas and is heated to 160°C. Post dilution, the sample goes through a heated line which is controlled with a Variac transformer such that the temperature at T4 is kept at 60°C. For the nvPM system, the pressure drop across the Dekati diluter (P1 – P2) is kept near zero which corresponds to a dilution factor of 8. If the pressure drop across the diluter remains constant, the dilution factor should remain fixed. The gauge pressure before the nvPM instrumentation (P3, Fig 10.) is kept near 0.8 psig to prevent flooding or reverse flow in the condensation particle counters (CPC). Where necessary, the bend radius of any tubing is greater than 10 times the inner diameter.

PAL has access to numerous commercial nvPM diagnostic equipment for size, number, and mass. The suite of instruments includes an Engine Exhaust Particle Sizer (TSI EEPS), Condensation Particle Counters (TSI CPC 3775/3776), Scanning Mobility Particle Sizers (TSI SMPS 3080/3082), Laser Induced Incandescence (Atrium LII-300), photoacoustic micro soot sensor (AVL MSS+), Cavity Attenuated Phase Shift extinction monitor (CAPS PMex), and a Cloud Condensation Nucleus (CCN) counter. For this paper, we present a schematic of the equipment limited to the following instruments: SMPS 3082, SMPS 3080, CPC 3775, and EEPS.

Fig. 12 shows a schematic of the nvPM instruments used in this work. Efforts are made to have a single path sampling circuit where at the end of the manifold is a pump set to 0-25 slpm controlled by a mass flow meter. The total flow rate is set greater than or equal to 20 slpm. Stainless steel barbed wye connectors are used to split the flow across various instruments. Conductive tubing is used at the inflow for all instrumentation to prevent electrostatic losses and silicone tubing is used at the exhaust. All instruments exhaust to a single manifold that vents to a filtration system prior to going to ambient. The SMPS scan times are set to 80 seconds up and 20 seconds down and use a sheath flow of 10 slpm. The SMPS 3082 uses a long 3081 differential mobility analyzer (DMA) which measures particles between 10 - 270 nm and the SMPS 3080 uses a 3085 nano DMA measuring between 2 – 80 nm at these sheath flows. Both SMPS systems use a CPC 3776 as their respective counter and operate at 1.5 slpm. The standalone CPC is a model 3775 which measures greater than 4 nm and a max particle number density of 10^7 #/cm^3. The EEPS serves as a redundant instrument which sizes and counts particles between 5.6 – 560 nm with coarser resolution of 32 bins (16 per decade) based on their electrical mobility.

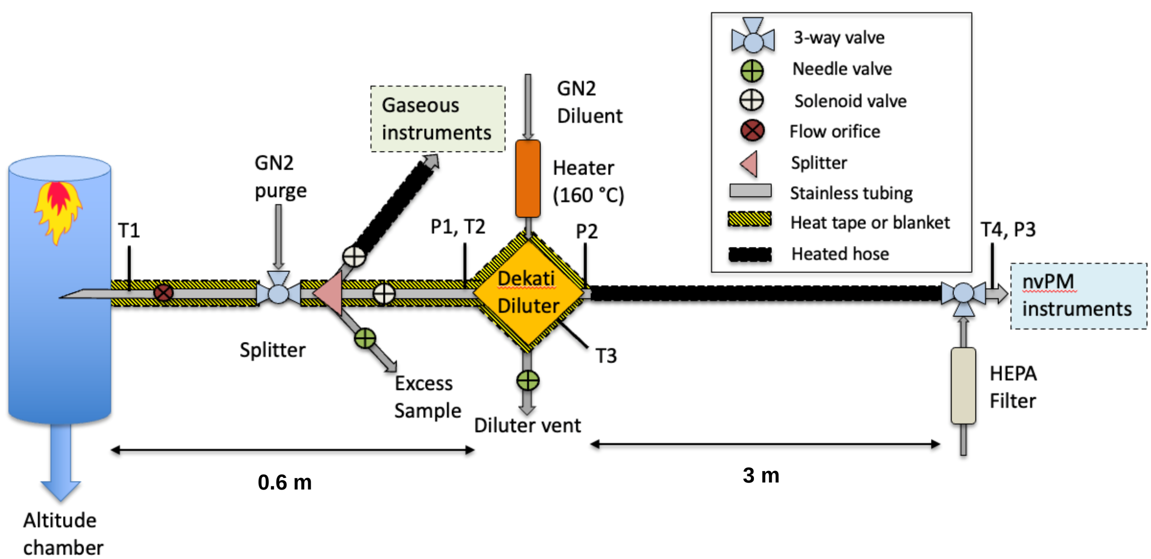

Fig. 10. Schematic of nvPM transfer and dilution section.

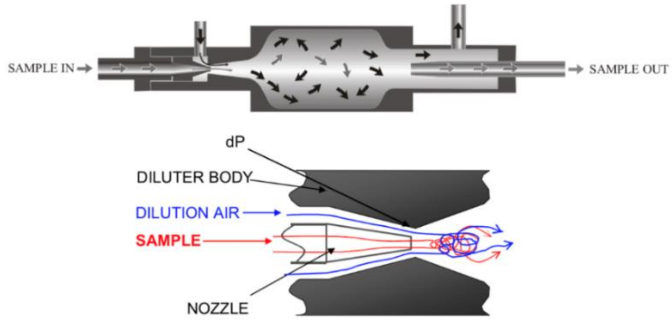

Fig. 11. Diagram of the ejector dilutor for the extractive sample diagnostics [13].

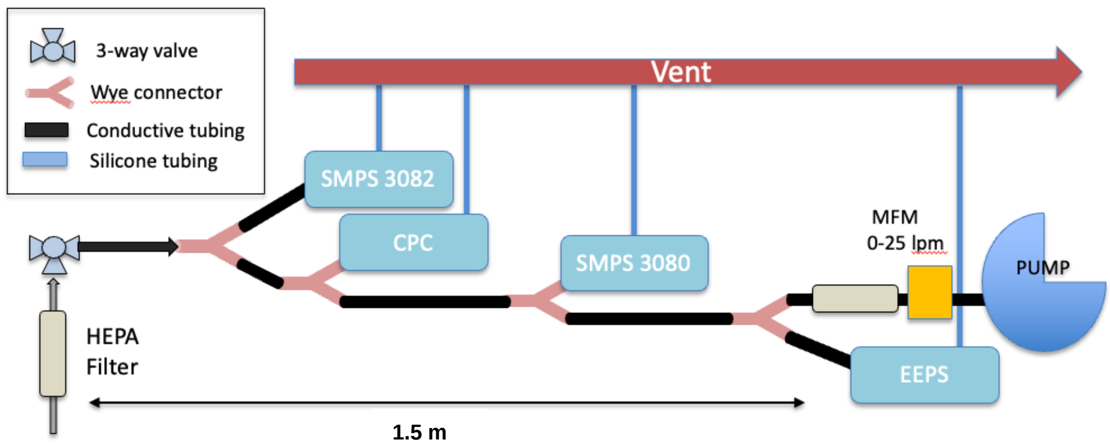

Fig. 12. Schematic of the extractive non-volatile particulates (nvPM) diagnostics suite.

V. Thermodynamic Prediction Code

A custom plume modeling code designated Scaling and Characterization ALgorithm for the Particulate Aerosol Lab (SCALPAL) was created and implemented to assist in describing contrail ice formation in the NASA PAL facility. Using peak water vapor saturation conditions, the ice production rate is first estimated. Using this information, the code then calculates the expected ice density at the optical measurement location in the tunnel by estimating the dilution of the nozzle plume by chamber co-flow.

The ice production rate is calculated by psychrometric evaluation of the nozzle plume characteristics as they mix with chamber co-flow. Using water vapor saturation characteristics of Parish & Putnam [14] the peak over saturation is estimated. The percentage of total humidity at the nozzle exit, which will freeze out during mixing, is then calculated. This is a derivative of the Schmidt-Appleman [15] technique. An illustration of this technique is shown in Fig. 13.

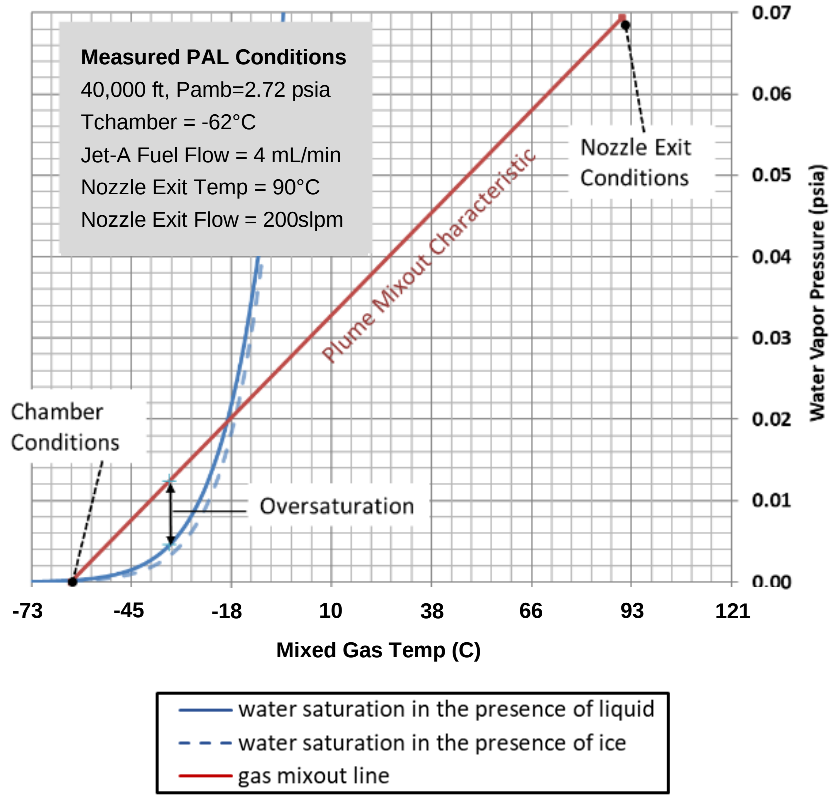

Fig. 13. Schmidt-Appleman curve for a set of common conditions in the PAL demonstrating the determination of oversaturation as a function of gas temperature in the chamber.

A custom-developed nozzle plume expansion code is used to estimate temperature and water vapor content throughout the test tunnel. The centerline decay of the jet is based on the model of Witze [16] which was shown by Bridges and Wernet [17] to agree well with PIV data collected at NASA GRC. We note that the figure of merit for SCALPAL is the plume temperature profile, whereas the Witze correlation estimates a normalized velocity profile. As an initial estimate, velocity and temperature were assumed to have similar characteristic profiles. Then, using temperature measurements made in PAL, the model radial profile distribution was ultimately calibrated to match these data via empirical correlation. A series of tests were conducted at the PAL facility for the purpose of surveying the temperature profile throughout the plume. The PAL flow field is considered axisymmetric. A thermocouple was moved to various locations in the plume to construct a two-dimensional temperature profile. The measurement locations were concentrated in regions of the plume that is well mixed, more than 10 diameters downstream of the nozzle exit, after the potential core has closed out. Line plots of the measured data and calibrated correlation for an example data point are shown in Fig. 14. The deviation at y values greater than 15 cm is noted and attributed to wall heating. Deviation in this area is considered acceptable because, while humid flow from the nozzle does migrate into this region, to do so it has already passed through its maximum oversaturation condition and therefore all vapor condensation processes will have gone to completion. No new ice is condensing in that area. Figure 15 shows an example contour plot of the resulting SCALPAL output ice density. With this result the integrated ice density across the diameter of the test tunnel may be calculated at any designated distance from the jet exhaust plane. This provides an estimate of ice density, based solely on thermodynamic state, suitable for comparison to the optically derived ice density measurements described in Section III. The code also provides a prediction of the gas velocity, gas temperature, and time-of-flight of particles throughout the entire flow field within the PAL chamber.

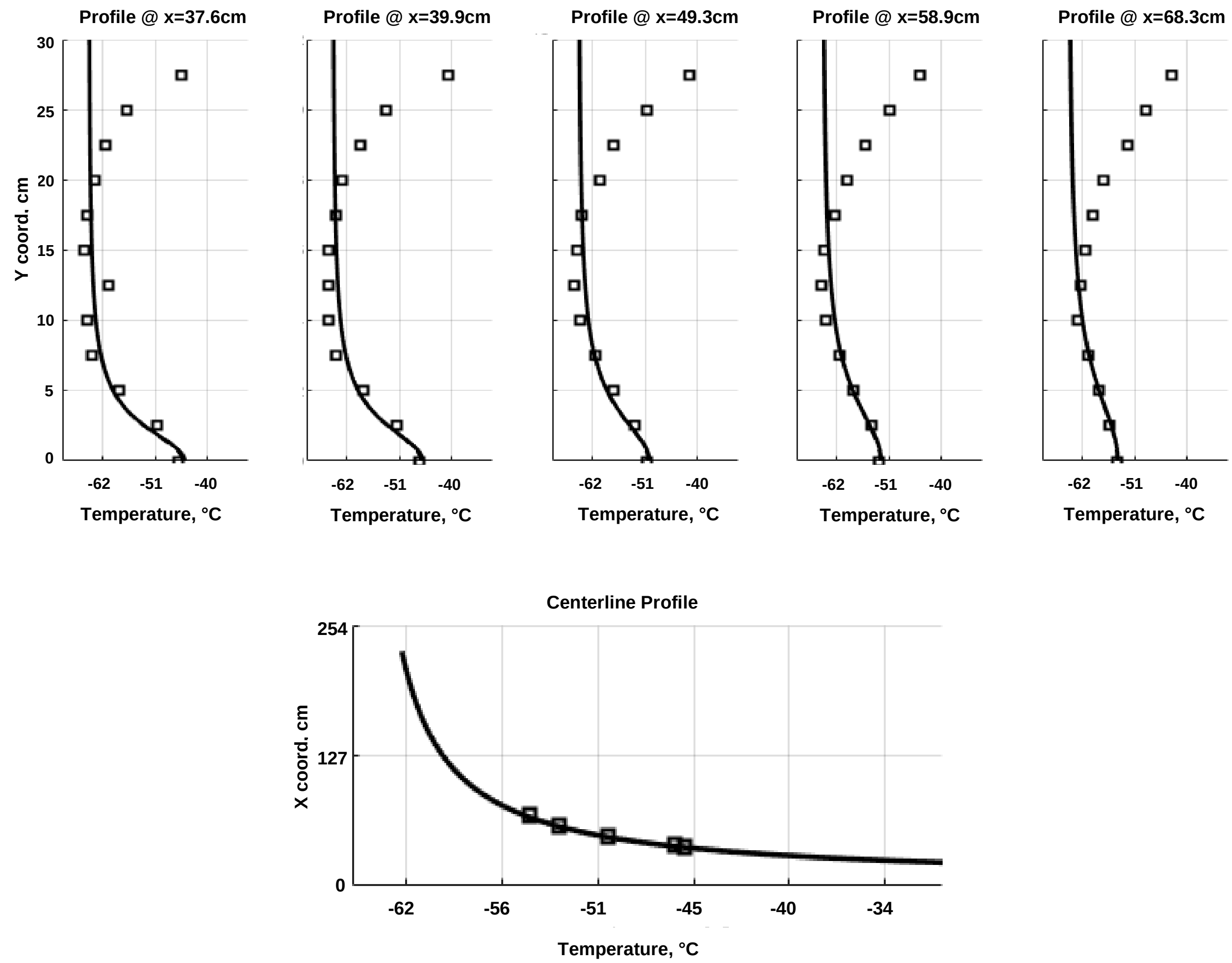

Fig. 14. Sample data showing agreement between measurement and custom-developed correlation for facility conditions: altitude = 43,000 ft, $T_{chamber}$ = -65°C, nozzle temp = 49°C. Symbols are the measurements, and solid lines are the correlations. The tunnel centerline is y=0 and the wall is y=30cm. Wall heating effects are not captured by the empirical model; however, the centerline profile along y=0 (bottom) shows excellent agreement.

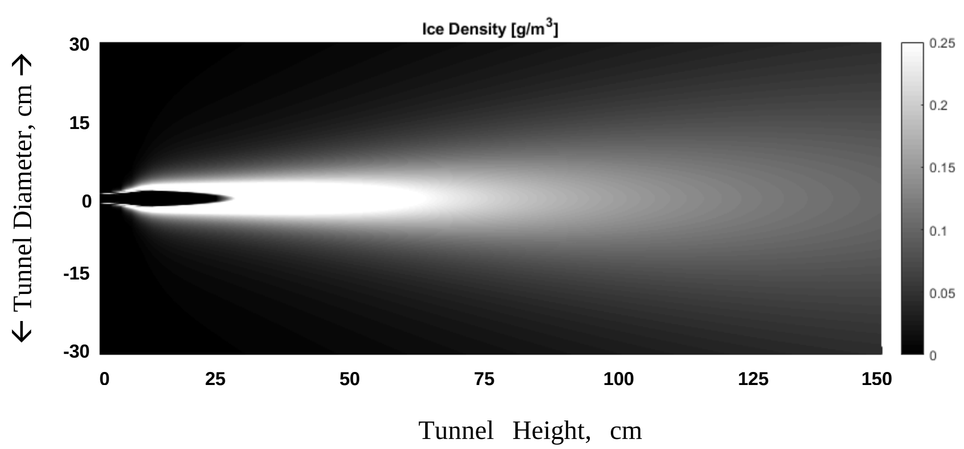

Fig. 15. An example contour plot of the resulting SCALPAL output ice density (g/m^3).

VI. Results and Discussion

Three different experiments were conducted to illustrate the effect of soot, fuel-to-air equivalence ratio, and simulated altitude (chamber pressure) on contrail ice particulate formation. These experiments were performed at common aircraft cruising altitudes and provide a demonstration of the PAL diagnostic capabilities. All optical ice particle measurements were acquired at the same axial location of 1.15 m or 64 jet diameters downstream of the 1.8 cm diameter nozzle exit. Soot measurements were sampled from inside the combustion chamber just before the combustion products enter the transition pipe as depicted in Fig. 4.

A. Effect of soot size and number density

Various fuels were burned to alter the size and quantity of soot produced in the combustor to investigate their effect on contrail formation. These included Jet-A, n-heptane, butanol, HEFA-SPK, and two different Fischer-Tropsch (FT) fuels. The yield sooting index (YSI) is a property of fuels that is related to the soot formation rate; a higher YSI indicates a greater sooting tendency relative to fuels of lower YSI [18]. The YSI values for Jet-A, n-heptane, and butanol are 60, 36, and 22, respectively. HEFA-SPK and FT fuels are SAF fuels that produce less soot than standard jet fuels due to their low aromatic content. One of the FT fuels is derived from coal while the other is derived from natural gas. HEFA-SPK is a Hydro-processed Esters and Fatty Acids Synthetic Paraffinic Kerosene fuel. Their exact YSI values are not known, but they should have lower YSI than Jet-A.

Soot and ice particle characteristics were measured for these six fuels using the extractive soot instruments and the Mie scattering diagnostic at chamber conditions of 40,000 ft (12 km) altitude, ambient temperature of -48°C, and nozzle exit temperature of 90°C. The total nozzle air flow was 205 slpm and the fuel flow rate was maintained constant at 4 mL/min for all six fuels. This resulted in equivalence ratios of approximately 0.24 for Jet-A and the three SAF fuels, 0.21 for n-heptane, and 0.18 for butanol. Figure 16 shows that the ice particle number density increases as soot numbers increase with the exception of butanol. Although the YSI of butanol is on the lower end of the tested fuels, the effects of oxygen on soot precursor chemistry are complex. Nativel et al. showed that acetylene and propargyl radicals increased with the addition of butanol to toluene mixture [19]. Acetylene and propargyl are well known soot precursors species, with the formation of propargyl being a key pathway in the formation of benzene. The conditions within the PAL combustor could therefore promote nvPM particle formation via excess acetylene and propargyl production relative to the other fuels tested. If we consider the non-butanol data points, Jet-A produces the largest amount of soot, followed by the three SAF fuels, while n-heptane produced the least amount of soot.

With the exception of butanol, Fig. 17 shows that ice particle size decreases with increasing soot numbers since there are more soot nucleation sites, resulting in smaller and more numerous ice particles for the same water content. Again, the chemistry of oxygenated species is complex, and products produced in the combustion of butanol could also change the hygroscopic and surface properties of the soot particles produced. Butanol could therefore lead to more hygroscopic soot particles leading to larger mean ice particle diameter. Figure 18 shows that there is not an obvious relationship between soot geometric mean size and ice particle size. The combustion process for each of these fuels produces a slightly different amount of water but the difference is less than 3%. The predicted ice densities from the thermodynamic prediction code are in the range 0.104-0.107 g/m^3 for all six fuels. The measured ice densities are plotted in Fig. 19 and most of the values fall slightly above this predicted range on average by about 8%. The ice density is very sensitive to the ambient gas temperature; small deviations from the predicted ice concentration is not surprising since the temperature of the chamber could easily vary by several degrees from that predicted by the plume model. If the ambient temperature was 1°C colder than the temperature measured by the chamber thermocouple, the predicted ice density for Jet-A would be 0.117 g/m^3 instead of 0.107 g/m^3.

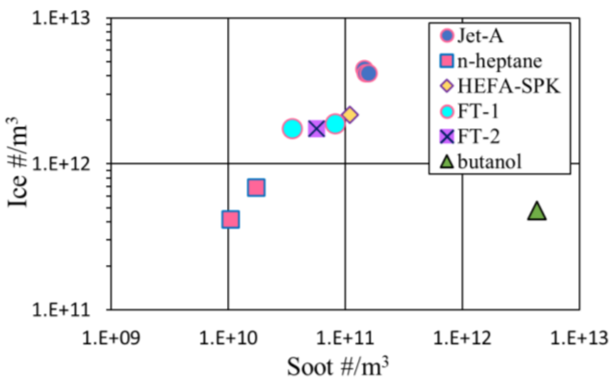

Fig. 16. Ice particle number density versus soot particle number density for various fuels at 40,000 ft and -48°C ambient conditions and a nozzle temperature of 90°C.

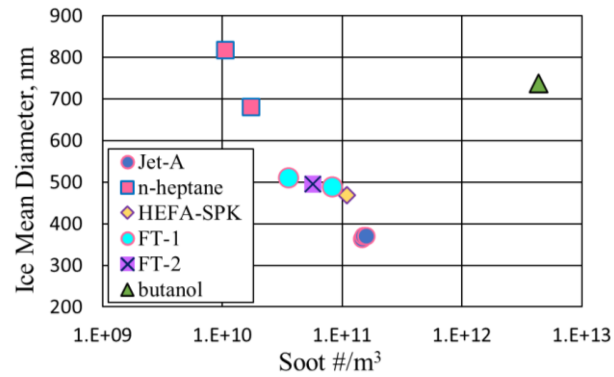

Fig. 17. Ice particle mean diameter versus soot particle number density for various fuels at 40,000 ft and -48°C ambient conditions and a nozzle temperature of 90°C.

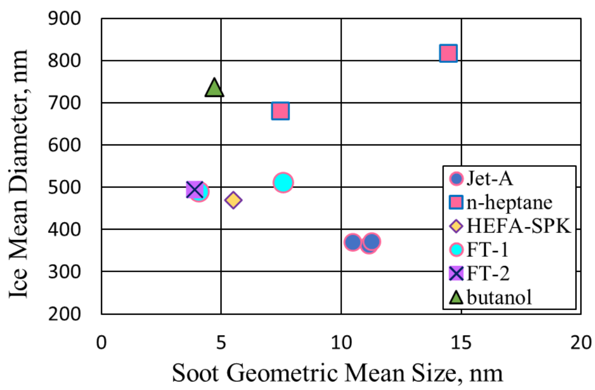

Fig. 18. Ice particle mean diameter versus geometric mean diameter of soot particles for various fuels at 40,000 ft and -48°C ambient conditions and a nozzle temperature of 90°C.

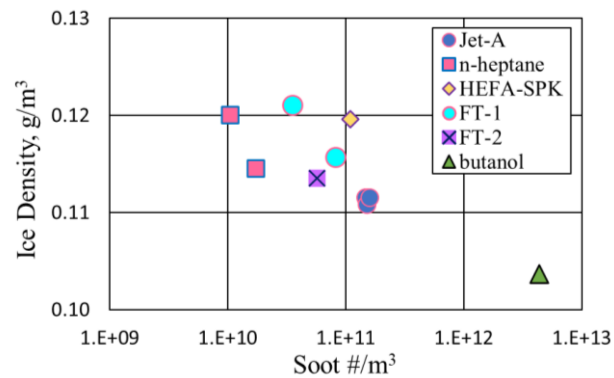

Fig. 19. Ice mass density versus soot particle number density for various fuels at 40,000 ft and -48°C ambient conditions and a nozzle temperature of 90°C.

B. Effect of fuel-to-air equivalence ratio

The fuel flow rate of three fuels (Jet-A, n-heptane, and butanol) was varied to provide an equivalence ratio (Φ) range from 0.24 to 0.36 to study the effect of this parameter on the contrail ice particle formation. Ice particle characteristics were measured using the Mie scattering diagnostic at chamber conditions for an altitude of 35,000 ft (10.7 km), ambient temperature of -54°C, and nozzle exit temperature nominally 150°C (this temperature changed slightly with changes in Φ). The total nozzle air flow was 160 slpm. The soot diagnostic equipment was unavailable at the time this experiment was conducted; therefore, only ice particle measurements are presented. The ice particle number density increases with increasing equivalence ratio while the mean diameter falls off slightly as shown in Figs. 20 and 21, respectively. The size and number density of the ice particles formed in the contrail for n-heptane and butanol are nearly identical, while the Jet-A contrail ice particles tend to be smaller and more numerous. There is a large amount of scatter in the Jet-A data at Φ = 0.27 but less scatter at the higher Φ values. Upon further inspection of the facility data, it was observed that the burner temperature increased from 410°C to 435°C and the nozzle exit temperature increased from 145°C to 159°C from the first to the last of the data points at Φ = 0.27. The burner and nozzle temperature did not vary as much for the remaining data. This shows that the contrail particle development is sensitive to these two values. The burner temperature likely influences the soot production while the nozzle temperature affects the thermodynamic state in the flow field. Figure 22 shows the measured and predicted ice density as a function of equivalence ratio. The measured values match the predictions within 6% deviation or less.

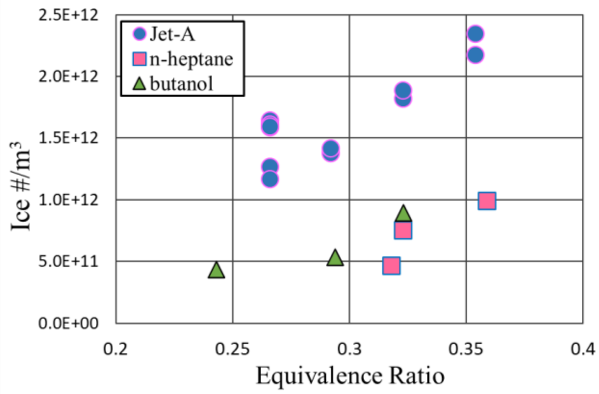

Fig. 20. Ice particle number density versus fuel-to-air equivalence ratio for various fuels at 35,000 ft and -54°C ambient conditions and a nozzle temperature of 150°C.

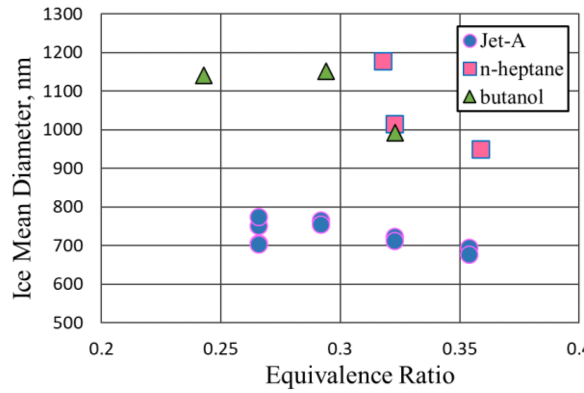

Fig. 21. Ice particles mean diameter versus fuel-to-air equivalence ratio for various fuels at 35,000 ft and -54°C ambient conditions and a nozzle temperature of 150°C.

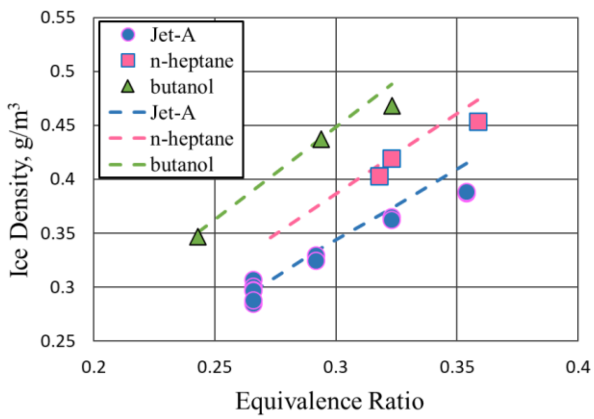

Fig. 22. Ice mass density versus fuel-to-air equivalence ratio for various fuels at 35,000 ft and -54°C ambient conditions and a nozzle temperature of 150°C. Measured values (circles) are compared with thermodynamic predictions (dashed lines).

C. Effect of altitude

The altitude of the PAL chamber was varied from 20,000 ft to 45,000 ft (6 km to 14 km) while maintaining a constant ambient temperature of -68°C to study the effect of altitude on the contrail ice particle formation. Jet-A fuel was maintained at a flow rate of 4mL/min for this experiment. The nozzle exit temperature was 95°C and the total nozzle air flow was 300 slpm. The ice particle characteristics were measured with the Mie scattering diagnostics; however, soot measurements were not acquired for this experiment. The ice particle number density shown in Fig. 23 stays roughly constant at approximately $1.7 \times 10^{13}/m^3$ over this range of altitudes. The combustion and the soot are unaffected by changes in the chamber pressure since the combustion chamber is isolated from the altitude chamber by two orifices. This is probably why the ice number density also does not change. However, ice mass density increases by a factor of four when going from 45,000 ft down to 20,000 ft as shown in Fig. 24. The higher ice density is accounted for by an increase in particle size. The ice density thermodynamic prediction is shown by the dashed line. The measured values match the prediction very well for all altitudes except the lowest one. The thermodynamic code was calibrated to the PAL chamber via thermocouple sweeps over a limited range of conditions which never went below an altitude of 35,000 ft (10.7 km). The deviation between the data and prediction may indicate that the code needs to be refined with additional calibration data at lower altitudes.

To determine if it might be a calibration issue, ice density measurements were compared to the prediction code results for conditions both inside and outside of the calibrated range. Ice particulate data were gathered from experiments spanning a one-year period and covering the full range of altitudes covered in this experiment, and as many different temperatures and ice density values as possible. The measured versus predicted ice density for this large sampling of data points is shown in Fig. 25 where the dashed line indicates perfect correlation. Surprisingly, the points with the largest deviation did not show a correlation with low altitude conditions. The spread of the data increases with increasing water concentration, but overall, there is good correlation between the data and prediction. It is still a useful exercise to refine the prediction code calibration with additional thermocouple measurements at more chamber conditions.

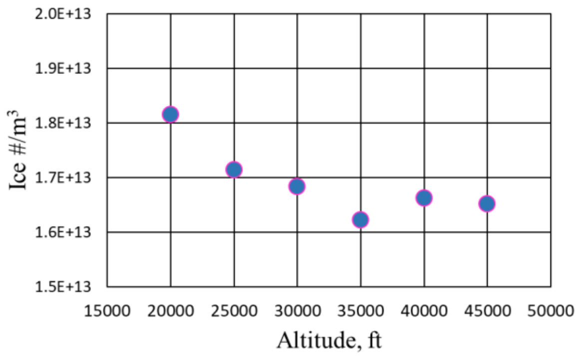

Fig. 23. Ice particle number density versus altitude for Jet-A at -68°C ambient temperature and a nozzle temperature of 95°C.

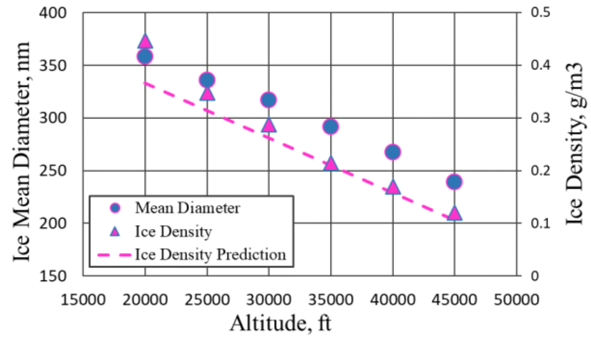

Fig. 24. Ice particle mean diameter (left axis) and ice density (right axis) versus altitude for Jet-A at -68°C ambient temperature and 95°C nozzle temperature. Ice density prediction is shown by the dashed line.

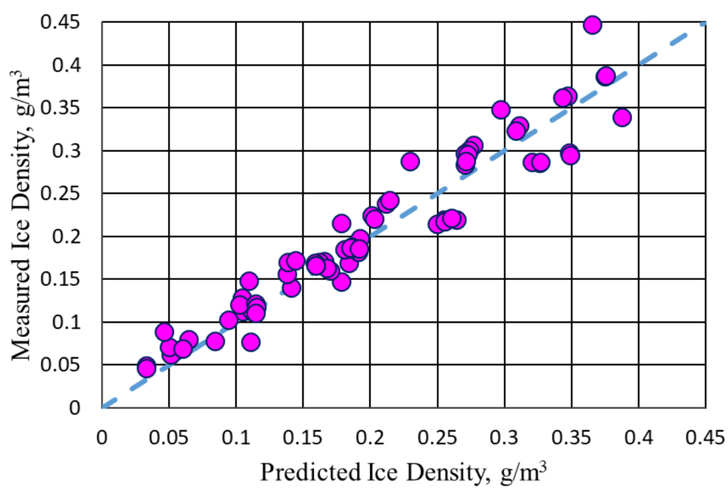

Fig. 25. Measured ice density compared to ice density predicted by the thermodynamic plume similarity code. All data is for Jet-A fuel at a variety of conditions acquired over a one-year period.

VII. Conclusion

The Particulate Aerosol Laboratory is a contrails research facility at the NASA Glenn Research Center. This paper provides details about the PAL, including the available controls, equipment, and diagnostics in the facility. An optical Mie scattering diagnostic measures mean ice particle size, number density, and ice mass density at an axial plane downstream of the nozzle exit. It enables measurement of ice particulates in the size range and concentrations typically found in upper troposphere flight corridors (diameter > 50nm and ice density > 0.04 g/m^3). A suite of non-volatile particulates diagnostic equipment provides soot measurements at the exit of the burner. A custom thermodynamic plume modeling code is available to assist in estimating the flow field and gas mix out in the NASA PAL facility. This model provides an estimate of ice density, based solely on thermodynamic state, suitable for comparison to the optically derived ice density measurements. The non-intrusive Mie scattering diagnostic plus extractive particulate instruments provide a suite of diagnostics to characterize exhaust plumes in the PAL facility. These diagnostics were used to study the effect of soot, fuel-to-air equivalence ratio, and altitude on contrail formation at a range of typical aircraft flight conditions using a series of fuels that produce varying amounts of soot. Increasing the soot number density while keeping the ice mass density constant results in smaller contrail ice particles at higher concentrations. The diameter of the ice particles was shown to have no correlation with the size of the soot particles. Increasing equivalence ratio produces more soot and water from the richer combustion conditions; therefore, the ice particle number density increases as well. The ice mean diameter decreased slightly with increasing equivalence ratio. Increasing altitude results in higher ice mass density in the contrail due to the lower ambient pressure. The main parameter that changes to accommodate the additional ice density is the particle size; the ice number density was mostly unaffected by a change in altitude. The combustion process, and therefore the soot, are not affected by a change in altitude so it is no surprise that the ice particle number density remains unaffected as well. These three experiments appear to support the conclusion that ice particle number density is affected most significantly by the soot number density, while the ice particle size is governed mostly by the ice density present in the plume. Comparisons between the measured ice density and the thermodynamic prediction agreed very well (within 6% or better) for most of the data in these three experiments. Observing data from a one-year period covering a wider range of conditions showed that the ice density data correlates well with the model prediction, although the spread in the data increases with increasing ice water content.

Acknowledgments

NASA's Aeronautics Research Mission Directorate (ARMD) supports this work.

References

[1] Button, K., "Curbing Contrails," *AIAA Aerospace America*, May 2021, https://aerospaceamerica.aiaa.org/features/curbing-contrails/

[2] Lee, D. S., et al., "The contribution of global aviation to anthropogenic climate forcing for 2000 to 2018," *Atmos. Environ*., Vol. 244, No. 117834, 2021, pp. 1-29. https://doi.org/10.1016/j.atmosenv.2020.117834

[3] Voigt, C., Kleine, J., Sauer, D., Moore, R. H., et al., "Cleaner burning aviation fuels can reduce contrail cloudiness," *Communications Earth and Environment*, Vol. 2, No. 114, 2021, pp. 1-10. https://doi.org/10.1038/s43247-021-00174-y

[4] Bräuer, T., Voigt, C., Sauer, D., Kaufmann, S., Hahn, V., Scheibe, M., Schlager, H., Huber, F., Le Clerq, P., Moore, R. H., and Anderson, B. E., "Reduced ice number concentrations in contrails from low-aromatic biofuel blends," *Atmos. Chem. Phys*., Vol. 21, 2021, pp. 16817-16826.

[5] Tacina, K. M., and Heath, C. M., "Evolution of Combustion-Generated Particles at Tropospheric Conditions," *Proceedings of the ASME Turbo Expo 2010: Power for Land, Sea and Air*, Vol. 2, Paper No. GT2010-23689, American Society of Mechanical Engineers, Glasgow, UK, 2010, pp. 1289–1299.
doi: 10.2514/1.C033040

[6] Wong, H. W., Beyersdorf, A. J., Heath, C. M., Ziemba, L. D., Winstead, E. L., Thornhill, K. L., Tacina, K. M., Ross, R. C., Albo, S. E., Bulzan, D. L., Anderson, B. E., and Miake-Lye, R. C., "Laboratory and modeling studies on the effects of water and soot emissions and ambient conditions on the properties of contrail ice particles in the jet regime," *Atmos. Chem. Phys*., Vol. 13, Oct 2013, pp. 10049-10060.

[7] Bateman, J. B., Weneck, E. J., and Eshler, D. C., "Determination of Particle Size and Concentration from Spectrophotometric Transmission," *J of Colloid Sciences*, Vol. 14, 1959, pp. 308-329.

[8] Maron, S. H., Pierce, P. E., and Ulevitch, I. N., "Determination of Latex Particle Size by Light Scattering," *J of Colloid Sciences*, Vol. 18, 1963, pp. 470-482.

[9] Cashdollar, K. L., Lee, C. K., and Singer, J. M., "Three-wavelength light transmission technique to measure smoke particle size and concentration," *Applied Optics*, Vol. 18, No. 11, 1979, pp. 1763-1769.

[10] Swanson, N. L., Billard, B. D., and Gennaro, T. L., "Limits of optical transmission measurements with application to particle sizing techniques," *Applied Optics*, Vol. 38, No. 27, 1999, pp. 5887-5893.

[11] Bohren, C. F., and Huffman, D. R., *Absorption and Scattering of Light by Small Particles*, John Wiley, New York, 1983.

[12] Mätzler, C., "MATLAB Functions for Mie Scattering and Absorption, Version 2" Research Report No. 2002-11, Institut für Angewandte Physik, Bern, 2002, pp. 1-24.

[13] Dekati Diluter User Manual, v 5.60, Dekati Ltd., Kangasala, Finland, 2019.

[14] Parish, O. O., and Putnam, T. W., "Equations for the Determination of Humidity from Dewpoint and Psychrometric Data," NASA/TN D-8401, 1977, pp. 1-23.

[15] Appleman, H., "The Formation of Exhaust Condensation Trails by Jet Aircraft," *Bulletin American Meteorological Society*, Vol. 34, No. 1, 1953, pp. 14-20.
[16] Witze, P. O., "Centerline Velocity Decay of Compressible Free Jets," *AIAA Journal*, Vol. 12, No. 4, 1974, pp. 417-418.
[17] Bridges, J. and Wernet, M. P., "The NASA Subsonic Jet Particle Image Velocimetry (PIV) Dataset, NASA/TM 2011-216807, 2011, pp. 1-49.
[18] Montgomerty, M. J., Das, D. D., McEnally, C. S., and Pfefferle, L. D., "Analyzing the robustness of the yield sooting index as a measure of sooting tendency," *Proceedings of the Combustion Institute*, Vol. 37, No. 1, 2019, pp. 911-918.
[19] Nativel, D., Shao C., Cooper, S. P., Petersen, E. L., Schulz, C., Fikri, M., and Peukert, S., "Impact of Methanol and Butanol on Soot Formation in Gasoline Surrogate Pyrolysis: A Shock-Tube Study," *J Phys Chem A*, Vol. 127, No. 5, 2023, pp. 1259-1270.